Identification of Radiopure Titanium for the LZ Dark Matter Experiment and Future Rare Event Searches

D.S. Akerib,[1,2] C.W. Akerlof,[3] D. Yu. Akimov,[4] S.K. Alsum,[5] H.M. Araújo,[6] I.J. Arnquist,[a] M. Arthurs,[3] X. Bai,[7] A.J. Bailey,[6,b] J. Balajthy,[8] S. Balashov,[9] M.J. Barry,[10] J. Belle,[11,c] P. Beltrame,[12] T. Benson,[5] E.P. Bernard,[13,14] A. Bernstein,[15] T.P. Biesiadzinski,[1,2] K.E. Boast,[16] A. Bolozdynya,[4] B. Boxer,[17,9] R. Bramante,[1,2] P. Brás,[18] J.H. Buckley,[19] V.V. Bugaev,[19] R. Bunker,[7,d] S. Burdin,[17] J.K. Busenitz,[20] C. Carels,[16] D.L. Carlsmith,[5] B. Carlson,[21] M.C. Carmona-Benitez,[22] C. Chan,[23] J.J. Cherwinka,[5] A.A. Chiller,[24] C. Chiller,[24] A. Cottle,[11] R. Coughlen,[7] W.W. Craddock,[1] A. Currie,[6,e] C.E. Dahl,[25,11] T.J.R. Davison,[12] A. Dobi,[10,f] J.E.Y. Dobson,[26] E. Druszkiewicz,[27] T.K. Edberg,[8] W.R. Edwards,[10] W.T. Emmet,[10] C.H. Faham,[10,g] S. Fiorucci,[10] T. Fruth,[16] R.J. Gaitskell,[23] N.J. Gantos,[10] V.M. Gehman,[10,h] R.M. Gerhard,[28] C. Ghag,[26] M.G.D. Gilchriese,[10] B. Gomber,[5] C.R. Hall,[8] S. Hans,[29] K. Hanzel,[10] S.J. Haselschwardt,[30] S.A. Hertel,[31] S. Hillbrand,[28] C. Hjemfelt,[7] M.D. Hoff,[10] B. Holbrook,[28] E. Holtom,[9] E.W. Hoppe,[a] J.Y-K. Hor,[20] M. Horn,[21] D.Q. Huang,[23] T.W. Hurteau,[14] C.M. Ignarra,[1,2] R.G. Jacobsen,[13] W. Ji,[1,2] A. Kaboth,[9,i] K. Kamdin,[10,13] K. Kazkaz,[15] D. Khaitan,[27] A. Khazov,[9] A.V. Khromov,[4] A.M. Konovalov,[4] E.V. Korolkova,[32] M. Koyuncu,[27] H. Kraus,[16] H.J. Krebs,[1] V.A. Kudryavtsev,[32] A.V. Kumpan,[4] S. Kyre,[30] C. Lee,[1,2,j] H.S. Lee,[33] J. Lee,[33] D.S. Leonard,[33] R. Leonard,[7] K.T. Lesko,[10] C. Levy,[34] F.-T. Liao,[16] J. Lin,[16,k] A. Lindote,[18] R.E. Linehan,[1,2] W.H. Lippincott,[11] X. Liu,[26] M.I. Lopes,[18] B. Lopez Paredes,[6] W. Lorenzon,[3] S. Luitz,[1] P. Majewski,[9] A. Manalaysay,[28] L. Manenti,[26] R.L. Mannino,[35] D.J. Markley,[11] T.J. Martin,[11] M.F. Marzioni,[12] C.T. McConnell,[10] D.N. McKinsey,[13,10] D.-M. Mei,[24] Y. Meng,[20] E.H. Miller,[7] E.Mizrachi,[1] J. Mock,[34,10] M.E. Monzani,[1,2] J.A. Morad,[28] B.J. Mount,[36] A.St.J. Murphy,[12] C. Nehrkorn,[30] H.N. Nelson,[30] F. Neves,[18] J.A. Nikkel,[9] J. O'Dell,[9] K. O'Sullivan,[10,13,1] I. Olcina,[6] M.A. Olevitch,[19] K.C. Oliver-Mallory,[10,13] K.J. Palladino,[5] E.K. Pease,[13,14] A. Piepke,[20] S. Powell,[17] R.M. Preece,[9] K. Pushkin,[3] B.N. Ratcliff,[1] J. Reichenbacher,[7] L. Reichhart,[26,m] C.A. Rhyne,[23] A. Richards,[6] J.P. Rodrigues,[18] H.J. Rose,[17] R. Rosero,[29] P. Rossiter,[32] J.S. Saba,[10] M. Sarychev,[11] R.W. Schnee,[7] M. Schubnell,[3] P.R. Scovell,[16] S. Shaw,[26,n] T.A. Shutt,[1,2] C. Silva,[18] K. Skarpaas,[1] W. Skulski,[27] M. Solmaz,[30] V.N. Solovov,[18] P. Sorensen,[10] V.V. Sosnovtsev,[4] I. Stancu,[20] M.R. Stark,[7] S. Stephenson,[28,o] T.M. Stiegler,[35] K. Stifter,[1,2] T.J. Sumner,[6] M. Szydagis,[34] D.J. Taylor,[21] W.C. Taylor,[23] D. Temples,[25] P.A. Terman,[35] K.J. Thomas,[10,p] J.A. Thomson,[28] D.R. Tiedt,[7] M. Timalsina,[7] W.H. To,[1,2,q] A. Tomás,[6] T.E. Tope,[11] M. Tripathi,[28] L. Tvrznikova,[14,13] J. Va'vra,[1] A. Vacheret,[6] M.G.D. van der Grinten,[9] J.R. Verbus,[23,1] C.O. Vuosalo,[5] W.L. Waldron,[10] R. Wang,[11] R. Watson,[10,13] R.C. Webb,[35] W.-Z. Wei,[24] M. While,[24] D.T. White,[30] T.J. Whitis,[1,2] W.J. Wisniewski,[1] M.S. Witherell,[10,13] F.L.H. Wolfs,[27] D. Woodward,[32] S. Worm,[9,r] J. Xu,[15] M. Yeh,[29] J. Yin,[27] and C. Zhang[24]

(The LUX-ZEPLIN (LZ) Collaboration)

[1]*SLAC National Accelerator Laboratory, P.O. Box 20450, Stanford, CA 94309-0450, USA*
[2]*Kavli Institute for Particle Astrophysics and Cosmology (KIPAC),*
Stanford University, 452 Lomita Mall, Stanford, CA 94309-4008, USA
[3]*University of Michigan, Randall Laboratory of Physics,*
450 Church Street, Ann Arbor, MI 48109-1040, USA
[4]*National Research Nuclear University MEPhI (NRNU MEPhI), 31 Kashirskoe shosse, Moscow, 115409, Russia*
[5]*University of Wisconsin-Madison, Department of Physics,*
1150 University Avenue Room 2320, Chamberlin Hall, Madison, WI 53706-1390, USA
[6]*Imperial College London, Physics Department, Blackett Laboratory, Prince Consort Road, London, SW7 2BW, UK*
[7]*South Dakota School of Mines and Technology, 501 East Saint Joseph Street, Rapid City, SD 57701-3901, USA*
[8]*University of Maryland, Department of Physics, College Park, MD 20742-4111, USA*
[9]*STFC Rutherford Appleton Laboratory (RAL), Didcot, OX11 0QX, UK*
[10]*Lawrence Berkeley National Laboratory (LBNL),*
1 Cyclotron Road, Berkeley, CA 94720-8099, USA
[11]*Fermi National Accelerator Laboratory (FNAL), P.O. Box 500, Batavia, IL 60510-5011, USA*
[12]*SUPA, University of Edinburgh, School of Physics and Astronomy, Edinburgh, EH9 3FD, UK*
[13]*University of California (UC), Berkeley, Department of Physics,*
366 LeConte Hall MC 7300, Berkeley, CA 94720-7300, USA
[14]*Yale University, Department of Physics, 217 Prospect Street, New Haven, CT 06511-8499, USA*
[15]*Lawrence Livermore National Laboratory (LLNL),*
P.O. Box 808, Livermore, CA 94551-0808, USA
[16]*University of Oxford, Department of Physics, Oxford, OX1 3RH, UK*
[17]*University of Liverpool, Department of Physics, Liverpool, L69 7ZE, UK*
[18]*Laboratório de Instrumentação e Física Experimental de Partículas (LIP),*
Department of Physics, University of Coimbra, Rua Larga, 3004-516, Coimbra, Portugal

^{19}*Washington University in St. Louis, Department of Physics,*
One Brookings Drive, St. Louis, MO 63130-4862, USA
^{20}*University of Alabama, Department of Physics & Astronomy,*
206 Gallalee Hall, 514 University Boulevard, Tuscaloosa, AL 34587-0324, USA
^{21}*South Dakota Science and Technology Authority (SDSTA),*
Sanford Underground Research Facility, 630 East Summit Street, Lead, SD 57754-1700, USA
^{22}*Pennsylvania State University, Department of Physics,*
104 Davey Lab, University Park, PA 16802-6300, USA
^{23}*Brown University, Department of Physics, 182 Hope Street, Providence, RI 02912-9037, USA*
^{24}*University of South Dakota, Department of Physics,*
414 East Clark Street, Vermillion, SD 57069-2307, USA
^{25}*Northwestern University, Department of Physics & Astronomy,*
2145 Sheridan Road, Evanston, IL 60208-3112, USA
^{26}*University College London (UCL), Department of Physics and Astronomy, Gower Street, London, WC1E 6BT, UK*
^{27}*University of Rochester, Department of Physics and Astronomy, Rochester, NY 14627-0171, USA*
^{28}*University of California (UC), Davis, Department of Physics,*
One Shields Avenue, Davis, CA 95616-5270, USA
^{29}*Brookhaven National Laboratory (BNL) P.O. Box 5000, Upton, NY 11973-5000, USA*
^{30}*University of California (UC), Santa Barbara, Department of Physics,*
Broida Hall, Santa Barbara, CA 93106-9530, USA
^{31}*University of Massachusetts, Department of Physics,*
1126 Lederle Graduate Research Tower (LGRT), Amherst, MA 01003-9337, USA
^{32}*University of Sheffield, Department of Physics and Astronomy, Sheffield, S3 7RH, UK*
^{33}*IBS Center for Underground Physics (CUP), 70,*
Yuseong-daero 1689-gil, Yuseong-gu, Daejeon, Korea
^{34}*University at Albany (SUNY), Department of Physics,*
1400 Washington Avenue, Albany, NY 12222-1000, USA
^{35}*Texas A&M University, Department of Physics and Astronomy,*
4242 TAMU, College Station, TX 77843-4242, USA
^{36}*Black Hills State University, School of Natural Sciences,*
1200 University Street, Spearfish, SD 57799-0002, USA
(Dated: February 15, 2017)

The LUX-ZEPLIN (LZ) experiment will search for dark matter particle interactions with a detector containing a total of 10 tonnes of liquid xenon within a double-vessel cryostat. The large mass and proximity of the cryostat to the active detector volume demand the use of material with extremely low intrinsic radioactivity. We report on the radioassay campaign conducted to identify suitable metals, the determination of factors limiting radiopure production, and the selection of titanium for construction of the LZ cryostat and other detector components. This titanium has been measured with activities of ^{238}U$_e$ <1.6 mBq/kg, ^{238}U$_l$ <0.09 mBq/kg, ^{232}Th$_e$ = 0.28±0.03 mBq/kg, ^{232}Th$_l$ = 0.25 ± 0.02 mBq/kg, ^{40}K <0.54 mBq/kg, and ^{60}Co <0.02 mBq/kg (68% CL). Such low intrinsic activities, which are some of the lowest ever reported for titanium, enable its use for future dark matter and other rare event searches. Monte Carlo simulations have been performed to assess the expected background contribution from the LZ cryostat with this radioactivity. In 1,000 days of WIMP search exposure of a 5.6-tonne fiducial mass, the cryostat will contribute only a mean background of 0.160 ± 0.001(stat)± 0.030(sys) counts.

[a] Pacific Northwest National Laboratory, P.O. Box 999, Richland, WA 99352-0999, USA; non-LZ Collaboration

[b] Now at: Instituto de Fsica Corpuscular (IFIC), University of Valencia and CSIC, Parque Cientfico, C/Catedrático José, Beltrán, 2, E-46980 Paterna, Spain

[c] Also at: Belle Aerospace Corporation (BAC), Wheaton, IL 60189-7059, USA

[d] Now at: Pacific Northwest National Laboratory, P.O. Box 999, Richland, WA 99352-0999, USA

[e] Now at: HM Revenue and Customs, 100 Parliament Street, London, SW1A 2BQ, UK

[f] Now at: Zenysis Technology, 535 Mission Street Floor 14, San Franciso, CA 94105-3253, USA

[g] Now at: LinkedIn, 2029 Stierlin Court, Mountain View, CA 94043-4655, USA

[h] Now at: Cainthus, Otherlab, 701 Alabama Street, San Francisco, CA 94110-2022, USA

[i] Also at: Royal Holloway, University of London, Department of Physics, Egham Hill, Egham, Surry, TW20 0EX, UK

[j] Now at: IBS Center for Underground Physics (CUP), 70, Yuseong-daero 1689-gil, Yuseong-gu, Daejeon, Korea

[k] Now at: University of California (UC), Berkeley, Department of Physics, 366 LeConte Hall MC 7300, Berkeley, CA 94720-7300, USA

[l] Now at: Insight Data Science, 260 Sheridan Avenue Suite 310, Palo Alto, CA 94306-2010, USA

[m] Now at: IMS Nanofabrication AG, Wolfholzgasse 20-22, 2345 Brunn am Gebirge, Austria

1. Introduction

Direct dark matter searches attempt to measure the interaction of Weakly Interacting Massive Particles (WIMPs) with an atomic nucleus, a process not yet observed. The very nature of this low-energy rare-event search demands extremely low background event rates in the signal region of interest. In recent leading experimental searches, the background has been dominated by the decay of naturally occurring radioactive contamination present within the materials used to construct the detectors, primarily ^{238}U, ^{232}Th, ^{40}K, and ^{60}Co. To achieve the design sensitivity, the control of such radioactivity is fundamental not only to direct dark matter experiments, but to rare event searches in general, requiring extensive radioassay campaigns to select suitable construction materials.

LZ (LUX-ZEPLIN) is a second generation dark matter experiment, presently under construction [1]. It will feature a two-phase xenon time projection chamber (TPC), containing approximately 7 tonnes of active liquid xenon (LXe) [2]. The total load of 10 tonnes of liquid xenon and other detector components will be held in a cryostat made from two nested vessels—the inner vessel contains the cold xenon whilst the outer vessel enables a vacuum region for thermal insulation. The material from which the cryostat is fabricated must be suitable for operation at cryogenic temperatures, must have mechanical properties that comply with international codes regulating the materials for pressure vessel fabrication, must not be prohibitively expensive and must be extremely radiopure.

Historically, dark matter searches have used cryostats made from stainless steel or electroformed oxygen-free high conductivity (OFHC) copper. Stainless steel is inexpensive, readily satisfies mechanical constraints with its high tensile strength, and vessels are straightforward to manufacture. However, ^{238}U and ^{232}Th content can be significant and highly variable and levels of ^{40}K and ^{60}Co are typically high. Copper is usually found to be considerably more radiopure, but thicker vessels are required relative to stainless steel when manufacturing pressure vessels for equivalent mechanical strength. The ZEPLIN-III experiment, one of the predecessors to LZ, used a low-activity copper cryostat containing 12 kilograms of

n Corresponding author: sally.shaw.13@ucl.ac.uk
o Now at: Deepgram, 148 Townsend Street, San Francisco, CA, 94107-1919, USA
p Corresponding author: thomas250@llnl.gov; Also at: University of California (UC), Berkeley, Department of Nuclear Engineering, 4155 Etcheverry Hall MC 1730, CA 94720-1730, USA; now at: Lawrence Livermore National Laboratory (LLNL), P.O. Box 808, Livermore, CA 94551-0808, USA
q Now at: California State University, Stanislaus, Department of Physics, 1 University Circle, Turlock, CA 95382-3200, USA
r Now at: University of Birmingham, Particle Physics Group, School of Physics and Astronomy, Edgbaston, Birmingham, B15 2TT, UK

LXe [3, 4]. For larger experiments at the tonne-scale and beyond, thick cryostats not only impact total radioactivity, but also attenuate internally-produced γ-ray and neutron backgrounds, acting to limit the effectiveness of veto detectors that may surround the primary target volume.

Titanium has previously been considered as an attractive alternative to stainless steel and copper. It has a high strength-to-weight ratio, is resistant to corrosion, and is already popular in the aerospace, metal finishing, oil refining and medical industries. It has a lower atomic number and therefore lower attenuation of low energy γ-radiation than stainless steel, should in principle contain very little ^{60}Co, and also benefits from little cosmogenic activation. This is significant since radioactive isotopes can be produced by neutron-induced spallation reactions whilst the material is still above ground. Stainless steel contains isotopes of iron, nickel and chromium that can be activated to form radioisotopes such as ^{56}Co, ^{58}Co, ^{54}Mn and ^{48}V [5], whilst in titanium, only the production of ^{46}Sc is a concern [6]. Although the LUX experiment [7–10], LZ's most recent predecessor, successfully manufactured and deployed a cryostat constructed from low-activity titanium to contain 350 kg of LXe [11], securing similarly radiopure material has proved non-trivial across the field of rare-event search experiments. The importance of constructing vessels of sufficient radiopurity has already been recognized as necessary for the next generation of neutrinoless double-beta-decay ($0\nu\beta\beta$) experiments [12].

To procure titanium for the manufacture of the LZ cryostat of similar or better radiopurity to that in LUX, an extensive R&D campaign has been conducted. This was necessary to ensure that reliably radiopure material could be sourced in sufficient quantities for LZ. The campaign has determined the requirements for procurement of reproducible radiopure titanium metal, included an extensive assay campaign of titanium samples (alongside stainless steel samples as an alternative) and, finally, selected suitable candidate materials. The measured radioactivities of screened samples have been used as input for detailed studies employing Monte Carlo simulations to model the LZ cryostat within the entire experiment. The impact of the intrinsic contamination in terms of background contribution to the WIMP search is determined, and this informs the selection of the most suitable sample for further confirmatory screening before procurement of the batch material for LZ.

2. Titanium Production and Contaminants

Titanium (Ti), a lightweight transition metal with atomic number 22, average atomic weight 47.90 and a density of 4510 kg/m^3, is the fourth most abundant metal on Earth, comprising 0.62% of the Earth's crust. Titanium production begins with the mining and refinement of ores, and involves exposure to coke, coal, oil and tar which can introduce significant contamination

of radioactive elements including uranium and thorium. However, titanium oxide ores are treated with chlorine gas to produce titanium tetrachloride ($TiCl_4$), which is found to have extremely low radiocontent after chemical treatment and filtering [13].

To produce metallic titanium, the $TiCl_4$ is reduced by liquid magnesium or sodium in a vessel filled only with argon to avoid oxygen or nitrogen contamination. This produces a porous titanium sponge, which is purified by leaching or heated vacuum distillation. There are typically no controls in place at this stage to limit contamination from surfaces or fluids in contact with the sponge, and thus variability in radioactivity of sponge products is expected.

Before melting the sponge, any alloys and scrap metals required are added by mechanical compaction. The use of these, where radioisotope contamination of source material is not traceable, constitutes the highest risk for introduction of radioactivity into the bulk material. At this stage the radiopurity may be greatly affected even if the purity has been preserved from the $TiCl_4$ through to the sponge.

Refinement of titanium sponge can be undertaken using either vacuum arc remelting (VAR) or electron beam cold hearth (EBCH) techniques. VAR is used for most commercial titanium and involves melting the metal under a vacuum in a crucible. A current is passed across a gap between an electrode consisting of compacted sponge and alloy and a smaller piece of the metal. This creates an arc and begins a continuous melting process. As the electrode melts, it must be lowered towards the bottom of the vessel, allowing control over the solidification rate, which affects the micro-structure of the titanium. The vacuum conditions allow any remaining gas contamination (e.g. N_2, O_2, H_2) to escape the titanium into the vacuum chamber. The resulting ingot is usually melted either once or twice more. Other impurities such as carbon, sulphur and magnesium that have a high vapour pressure will also be reduced in concentration. The disadvantages of VAR are that it is a slow process and nitrogen-rich low density particles survive as their residence time at sufficient temperatures is not long enough to melt them.

Electron beam remelting uses electron beams to heat and melt metals in a water-cooled copper crucible under a vacuum. In EBCH, cold hearth refers to a watercooled copper hearth in which the feedstock is drip melted, overflowing into a withdrawal mold. EBCH holds some advantages for manufacturers: it is a faster process as it involves fewer steps than traditional refinement implying fewer opportunities for further radiological contamination, its high yield, its flexibility in melting feedstock of any geometry and finally the possibility of producing ingots and slabs with a wide range of cross sections. A final and key advantage for applications such as low-background experiments is that EBCH exceeds other refinement methods in removing high density contaminants, as these sink to the bottom of the hearth and so do not reach the mold [14].

As part of the radioassay campaign for LZ, titanium of varying grades has been sampled in partnership with several manufacturers and at various stages of the production cycle beyond radiopure $TiCl_4$ (including sponge, slabs, and sheet), using both re-melting processes (VAR and EBCH), and with varying scrap concentrations (with the majority requested and delivered with 0% scrap).

3. Radioassay Campaign

3.1. Screening Techniques

The cryostat material assays have been primarily carried out by the Berkeley Low Background Facility using its surface screening detectors at the Lawrence Berkeley National Laboratory and the underground HPGe system MAEVE. Until November 2015, MAEVE was located underground (∼550 ft) at the Oroville Dam in Oroville, California, but has now been relocated to the Black Hills State University Underground Campus (BHUC) facility dedicated to low-background counting 4,850 ft underground at the Sanford Underground Research Facility (SURF) in Lead, South Dakota. MAEVE is an ORTEC HPGe 85% p-type detector in a low background cryostat, shielded by OFHC copper and lead. For samples of a few kg, the sensitivity after two weeks of counting reaches approximately 10 ppt U ($\approx$0.1 mBq/kg ^{238}U) and 25 ppt Th ($\approx$0.1 mBq/kg ^{232}Th), 20 ppb for K ($\approx$0.7 mBq/kg ^{40}K) and $\approx$0.03 mBq/kg for ^{60}Co. MAEVE counting efficiencies were modelled with a GEANT4 [15] simulation including precise geometry, accounting for sample dimensions and placement within the detector castle. The GEANT4 models were carefully verified with well-characterized, homogeneous, weakly radioactive sources to ensure the validity of the Monte Carlo simulations for both geometric placement, self-attenuation, and energy response of the HPGe crystal.

Measurements have also been performed at the Boulby Underground Laboratory in the UK, primarily using CHALONER, a 0.8 kg Canberra BE5030 Broad Energy Germanium (BEGe) detector. This instrument, with the advantage of its low energy threshold ($\approx$15 keV), was used to perform confirmation measurements, particularly of the low energy and low branching ratio lines close to the top of the ^{238}U and ^{232}Th decay chains. Low background HPGe detectors operated at the University of Alabama in a surface laboratory have also been utilized for this campaign. All detectors have been cross-calibrated with results from the assay of standard sources, and agree within stated systematic uncertainties.

All signal peaks detected with HPGe are passed for analysis, and multiple lines are measured to infer ^{238}U and ^{232}Th concentrations, as well as the lines from ^{60}Co, ^{137}Cs and other long-lived species. For ^{238}U it is standard to measure the decays of ^{226}Ra, ^{214}Pb and ^{214}Bi, and for ^{238}Th the decays of ^{228}Ac, ^{212}Bi, ^{212}Pb and ^{208}Tl. Rather than combining these lines to report single values for ^{238}U and ^{232}Th, we separately extract both early chain and late chain activities as manufacturing/chemical

processes may break secular equilibrium in the chains. This separation is necessary given the different energies and branching ratios of γ-rays throughout the chains, and more significantly, the impact on neutron production yields through both (α,n) processes and spontaneous fission. In the case of ^{238}U, we define the early part of the chain $(^{238}\text{U}_e)$ as containing any isotopes above ^{226}Ra $(T_{1/2} = 1600 \text{ yr})$. The late part of the chain $(^{238}\text{U}_l)$ is counted from ^{226}Ra and below. Another break in the U chain often occurs at ^{210}Pb $(T_{1/2} = 22 \text{ yr})$ and is also reported separately when available. Among the ^{238}U sub-chains, contributions from $^{238}\text{U}_l$ dominate LZ γ-ray and (α,n) backgrounds [16], whilst γ-rays and neutrons from fission of ^{238}U in $^{238}\text{U}_e$ are efficiently vetoed [17]. For the ^{232}Th chain, we define the early part of the chain $(^{232}\text{Th}_e)$ as coming from isotopes above ^{224}Ra and the late part of the chain $(^{232}\text{Th}_l)$ as coming from isotopes from ^{228}Th and below. Among the ^{232}Th sub-chains, roughly equal contributions to LZ γ-ray background arise from $^{232}\text{Th}_e$ and $^{232}\text{Th}_l$, whilst (α,n) backgrounds arise dominantly from $^{232}\text{Th}_l$.

Small samples of titanium have been subjected to direct mass spectroscopy for their U and Th content using an Agilent 7900 Inductively Coupled Plasma Mass Spectrometer (ICP-MS), operated at the Pacific Northwest National Laboratory (PNNL). Care was taken to avoid trace contamination of these small samples in handling, preparation and assay.

3.2. Radioassay Results

Titanium samples were secured for radioassay from several international manufacturers and suppliers, including VSMPO [18], TIMET [19], Supra Alloy [20], Honeywell [21] and PTG [22]. The samples were collected from stages throughout the manufacturing process with a focus on final processed sheet. TIMETAL®35A sheet samples, equivalent to ASTM Grade 1, showed the highest radiopurity in early measurements and so several were obtained. After rejection of samples with known high scrap content or where traceability of the sample through the manufacture process was compromised, 22 samples were selected for assay with the high sensitivity underground gamma spectroscopy detectors. The sample masses varied from approximately 0.5 kg to 10 kg and were cleaned prior to assay by etching with hydrofluoric and nitric acids. Several different types of titanium were measured: ASTM Grade 1 which is the highest grade purity of unalloyed titanium with a maximum oxygen content of 0.18%, ASTM Grade 2 which is also unalloyed but may contain a maximum oxygen content of up to 0.25%, porous titanium sponge created during the first stage of processing, and some finished nuts and bolts. The radioassay results from each of these samples are presented in Table I.

Validation of the ICP-MS assays was performed through comparison with inferred $^{238}\text{U}_e$ and $^{232}\text{Th}_e$ activities measured with γ-screening measurements of sample TIMET Sheet (4). ICP-MS can achieve higher sensitivity for some elements in particular matrixes, utilizes a much smaller sample mass, and requires a shorter measurement time than γ-screening measurement. However, ICP-MS can suffer systematic errors that are larger than those in γ-screening measurement, due to contamination of the smaller sample mass, and variation due to the sampling of a small fraction of a large mass. TIMET Sheet (4) is ASTM Grade 1 titanium with 0% scrap, and was produced with EBCH re-melting. Two samples of this material were assayed with ICP-MS: a large piece (TiLarge) separated into 3 pieces of 1 g each measured separately, and a small rectangular bar (TiSmall) measured once. A surface etch was performed on the TiLarge pieces to remove any surface contamination remaining after cleaning the samples. The etched material (TiLarge Etch) was retained and assayed separately to the bulk material (TiLarge Inner). The results of the assays are presented in Table II. Uncertainties reported for TiLarge use the standard deviation of the three samples as well as instrumental precision, whilst TiSmall uses instrumental precision only. ^{238}U results are consistent between samples, whilst ^{232}Th results show discrepancy particularly from the etched material, likely due to surface contamination from processing. The results from the the ICP-MS are generally in agreement with the LZ γ-screening measurements of 8 ± 2 mBq/kg of ^{238}U and <0.12 mBq/kg of ^{232}Th—indicating the successful control of systematic effects in the ICP-MS process.

In parallel with the titanium R&D, we maintained a programme to secure samples of stainless steel as a viable alternative for the LZ cryostat to mitigate risk of being unable to find a source of sufficiently radiopure titanium, or an inability to manufacture a sufficiently large quantity. Stainless steel samples were sourced from NIRONIT [24], suppliers for the GERDA [5], NEXT [23] and XENON100 [25] experiments. We also re-measured a selection of stainless steel samples previously measured by the GERDA and NEXT experiments for independent assay, finding activity levels consistent with theirs [5, 23]. The radioassay results of the 22 stainless steel samples are presented in Table III. NIRONIT samples were sourced from ThyssenKrupp (samples 2–6, 9 and 13) and Aperam (1, 7, 8, 11, 12).

3.3. Material Selection

Following the assays of all 22 Ti and 22 stainless steel samples, the highest and most reproducible radiopurity is found in ASTM Grade 1 titanium that contained 0% scrap and had been refined using EBCH technology. Of these, the lowest radioactivity is observed in material from TIMET Heat Number (HN) 3469, a single 15,000 kg slab of titanium, produced by TIMET at its Morgantown (Pennsylvania) mill. Results from a chemical analysis of this sample to measure concentrations of iron, carbon, oxygen and nitrogen are shown in Table IV.

A sample from TIMET HN3469, denoted HN3469-T, was screened at the Berkeley Low Background Facility

Table I: Radioassay results of 22 titanium samples (68% CL) from a variety of suppliers. Numbers in italics are 1σ upper limits. ^{210}Pb results are given where available; high activities were observed in TIMET sponges, identifying them as unsuitable. Systematic uncertainties are estimated to be up to 10% by comparing the cross-calibration results of the assay of standard sources.

Name	Type	^{238}U (mBq/kg) early	late	^{210}Pb	^{232}Th (mBq/kg) early	late	^{40}K (mBq/kg)
Supra Alloy Sheet (1)	ASTM Grade 1 Sheet	32	4.2	-	3.3	2.8	*<1.9*
Supra Alloy Sheet (2)	ASTM Grade 2 Sheet	110	*<2*	-	200	180	25
TIMET Sponge (1)	Sponge	25	*<2*	250	*<4.1*	*<4.1*	*<12*
TIMET Sponge (2)	Sponge	*<25*	*<2*	6200	*<4.1*	*<2.4*	*<15*
TIMET Sponge (3)	Sponge	*<25*	*<2*	*<62*	*<5.3*	*<1.6*	*<12*
TIMET Sponge (4)	Sponge	74	*<2*	120	*<4.1*	*<1.6*	*<12*
TIMET Sponge (5)	Sponge	*<12*	*<2*	740	*<4.1*	*<1.6*	*<12*
TIMET Sponge (6)	Sponge	74	*<4*	2500	*<5.3*	14	*<19*
TIMET Sponge (7)	Sponge	37	25	2500	12	5.7	*<12*
TIMET Sheet (1)	ASTM Grade 1 Sheet	11	*<0.62*	-	*<0.8*	*<0.6*	*<2.5*
TIMET Sheet (2)	ASTM Grade 1 Sheet	5	3.3	-	2.8	0.8	*<1.5*
TIMET Sheet (3)	ASTM Grade 1 Sheet	8.5	0.37	-	0.45	0.61	*<0.5*
TIMET Sheet (4)	ASTM Grade 1 Sheet	8.0	*<0.12*	-	*<0.12*	*<0.1*	*<0.6*
TIMET HN3469-T	ASTM Grade 1 Slab	*<1.6*	*<0.09*	-	0.28	0.23	*<0.5*
TIMET HN3469-M	ASTM Grade 1 Slab	2.8	*<0.10*	-	*<0.20*	0.25	*<0.7*
PTG Sheet (1)	ASTM Grade 1 Sheet	47	2.8	-	2.0	2.8	*<1.9*
PTG Sheet (2)	ASTM Grade 2 Sheet	*<9.9*	3.7	-	*<0.81*	2.4	*<2.2*
Bolts	Bolts	1300	*<6.2*	-	160	160	*<37*
Nuts/Washers	Nuts/Washers	520	*<8.6*	-	*<12*	81	*<62*
Honeywell Sheet	ASTM Grade 1 Sheet	3.7	4.7	-	1.5	1.6	*<1.5*
VSMPO Disc (10% scrap)	ASTM Grade 1 Metal	62	*<6.2*	-	*<4.1*	*<4.1*	*<31*
VSMPO Sponge	ASTM Grade 1 Sponge	17	12	-	*<4.1*	*<4.1*	*<6.2*

Table II: ICP-MS assay results of TIMET Sheet (4) titanium samples. Also shown for comparison are the ^{238}U$_e$ and ^{232}Th$_e$ (1 σ upper limits) results from γ-screening where uncertainties are statistical only and a systematic uncertainty of up to 10% is estimated by comparison of cross-calibration assays.

Sample	^{238}U (mBq/kg)	^{232}Th (mBq/kg)
TiLarge Inner	9.9 ± 0.2	0.12 ± 0.01
TiLarge Etch	9.9 ± 0.8	0.7 ± 0.2
TiSmall	9.8 ± 0.2	0.086 ± 0.003
HPGe	8.0 ± 2.0	*<0.12*

using MAEVE in May of 2015. This consisted of 10.1 kg of plates selected from the top portion of the single slab. A second sample taken from the middle (HN3469-M), was acquired and assayed in September of 2015 to confirm the uniform distribution of contamination. The radioactivities of both samples of this titanium stock were found to be consistent.

In both samples, each counted for approximately three weeks, the early uranium chain was non-detectable or barely detectable within the limited abilities of HPGe detectors to assay this portion of the decay chain via γ-ray spectroscopy. The late portion of the chain (at ^{226}Ra and below), however, is quite accessible via γ-ray spectroscopy due to both the branching ratio and detection efficiency for γ-rays emitted during the decay of constituent isotopes, and registered no detectable activity above background down to a few ppt. The ^{238}U$_l$ value

is based upon the 609 keV peak from ^{214}Bi and is consistent when compared to upper limits from other useful peaks in the late uranium chain, such as from ^{214}Pb (295, 352 keV) and ^{214}Bi (1764 keV). Both samples had detectable levels of the thorium series in both the early and late portions of the chain, consistent with secular equilibrium in both samples. The ^{232}Th$_l$ measurement is based upon the 238 keV γ-ray from ^{212}Pb, which is the strongest peak given the product of the detection efficiency of that γ-ray line and its branching ratio in the thorium chain. The assays are summarized in Table V.

In terms of cosmogenic activation there were several isotopes of scandium present, most of which are the result of cosmic ray-induced reactions with the five stable isotopes of titanium. Detected in the sample was ^{46}Sc (889, 1121 keV, $T_{1/2}$=84 days); as well as small amounts of ^{47}Sc (159 keV, $T_{1/2}$=3 days), ^{48}Sc (984, 1038, 1312 keV, $T_{1/2}$=44 hours), and ^{44,44m}Sc (271, 1157 keV, $T_{1/2}$=59 hours and 4 hours, the metastable state being the longer-lived). Screening results for ^{46}Sc are also listed in Table V, whilst the ^{47}Sc, ^{48}Sc, and ^{44,44m}Sc activities were not listed as their short half lives mean they essentially disappear over the course of the measurement. The reported value for ^{46}Sc was corrected to the start of counting for each of the samples. The cosmogenic production of ^{46}Sc can be mitigated by moving components underground as soon as possible after manufacture.

The activities reported here for TIMET HN3469 are among the lowest worldwide known to-date for titanium; the radiopurity is comparable to the LUX titanium (U$_l$<0.25 mBq/kg, Th$_l$<0.2 mBq/kg [11]), making

Table III: Radioassay results from the 13 stainless steel samples directly from NIRONIT, 3 from GERDA and 3 from NEXT. All limits are 1σ upper limits and systematic uncertainties are estimated to be up to 10% by comparing the cross-calibration results of the assay of standard sources. NIRONIT samples that were excluded following pre-screening due to their high ^{60}Co content were not assayed for early-chain contents. Samples (2–6) were selected for additional assay underground at SURF using Maeve primarily upon their lower ^{60}Co content. Published results from the GERDA and NEXT collaborations are included for comparison.

Name	^{238}U (mBq/kg) early	late	^{232}Th (mBq/kg) early	late	^{60}Co (mBq/kg)	^{40}K (mBq/kg)
NIRONIT (1)	7.3	0.35	1.1	4.0	14.5	0.53
NIRONIT (2)	1.2	0.27	0.12	0.49	1.6	<0.4
NIRONIT (3)	<1	0.54	0.49	1.1	1.7	<0.59
NIRONIT (4)	1.4	0.5	0.5	0.32	2.6	<0.5
NIRONIT (5)	1.1	0.38	0.81	0.73	5.6	<0.46
NIRONIT (6)	0.5	1.9	1.7	1.5	4.5	<0.5
NIRONIT (7)	-	1.1	-	4.1	8.2	<3.0
NIRONIT (8)	-	<0.6	-	<0.8	7.4	<3
NIRONIT (9)	-	<0.6	-	<0.9	6.5	<3
NIRONIT (10)	-	4	-	2.2	26	<4
NIRONIT (11)	-	<0.6	-	4.8	32	<2
NIRONIT (12)	-	<0.8	-	2.1	32	5
NIRONIT (13)	-	<1.4	-	<1.5	335	<4
GERDA D6	<5		<0.4		-	<0.002
published [5]	<0.6		<1.4		16.8 ± 2.4	<1.8
GERDA G1	<5		<0.4		-	<0.003
published [5]	<1.3		<2.6		45.5 ± 2.1	<2.8
GERDA G2	<5		<0.4		-	<0.003
published [5]	<0.86		<0.24		14.0 ± 0.1	< 0.93
NEXT 10 mm	7.46		<0.24		-	<0.63
published [23]	<21		<0.59		2.8 ± 0.2	<0.96
NEXT 15 mm	12.4		<0.24		-	<0.63
published [23]	<25		<0.69		4.4 ± 0.3	<1.0
NEXT 50 mm	12.4		<0.24		-	<0.63
published [23]	67 ± 22		2.1 ± 0.4		4.2 ± 0.3	<2.5

Table IV: Chemical analysis of two samples from TIMET HN3469-T, showing % weight of iron, carbon, oxygen and nitrogen in the titanium [26].

Sample	Fe	C	O	N
1	0.01	0.001	0.04	0.002
2	0.02	0.006	0.02	0.002

Table V: Results from γ-ray spectroscopy of TIMET titanium sample HN3469 for both top and middle samples. All limits are 1σ upper limits and uncertainties are statistical only. A systematic uncertainty of up to 10% has to be additionally assumed. Results were obtained with the Maeve detector and confirmed with ICP-MS and the Chaloner detector.

	Top	Middle
Date	May 2015	Sep. 2015
Sample mass	10.07 kg	8.58 kg
Livetime	23.9 days	20.8 days
^{238}U$_e$	<1.6	2.80 ± 0.15
^{238}U$_l$	<0.09	<0.10
^{232}Th$_e$	0.28 ± 0.03	<0.20
^{232}Th$_l$	0.23 ± 0.02	0.25 ± 0.02
^{40}K	<0.54	<0.68
^{60}Co	<0.02	<0.03
^{46}Sc	2.0 ± 0.1	2.7 ± 0.1

the campaign a success. Titanium from the HN3469 slab has been procured for the 2,292 kg LZ cryostat and cryostat support structures, as well as other internal structures amounting to ∼364 kg. The measured radioactivities in the cryostat materials used in other dark matter and $0\nu\beta\beta$ experiments are shown for comparison in Table VI. The cryostat material with the lowest radiopurity and most sensitive measurements is the copper used in the Majorana Demonstrator (MJD) $0\nu\beta\beta$ experiment, which is electroformed underground to ensure extremely low levels of contamination.

4. Cryostat Background

4.1. Overview of Backgrounds

Backgrounds from the cryostat may be categorised into two classes: electron recoils (ER) and nuclear recoils (NR). ER events can be discriminated against in a LXe TPC to greater than 99.5% efficiency, while NR events

may not as they are essentially signal-like. Neutron-induced NR are indistinguishable from WIMPs if only a single elastic scatter occurs within the LZ fiducial volume, unaccompanied by any other signal in other active veto volumes of the experiment. Leading LZ background sources include astrophysical neutrinos, intrinsic radioactivity in the Xe, and emission from every component in the experiment.

Radon emanation from the cryostat materials con-

Table VI: Radioactivities of cryostat material for a selection of dark matter and $0\nu\beta\beta$ experiments. Late chain ^{238}U & ^{232}Th activities are quoted due to the sparsity of data on early chain activities. Activities for ^{60}Co, ^{40}K, and ^{46}Sc are included where results are publicly available. Results from XENON100 and GERDA were reported as total activity and have been scaled by the given mass for comparison.

Experiment	Type	Mass (kg)	^{238}U (mBq/kg)	^{232}Th (mBq/kg)	^{60}Co (mBq/kg)	^{40}K (mBq/kg)	^{46}Sc (mBq/kg)
DarkSide50 [27]	SS	175	<1	<1	13.1 ± 1	-	-
XENON100 [25]	SS	74	<1.8	<0.03	5.4 ± 0.5	<9	-
XENON1T [28]	SS	870	2.4 ± 0.7	0.21 ± 0.06	<0.36	9.7 ± 0.8	2.7
ZEPLIN-III [29]	Cu	400	<6.22	<2.03	-	<0.32	-
EXO-200 [30]	Cu	5,901	<0.01	<0.003	-	<0.01	-
GERDA [31]	Cu	16,000	0.017 ± 0.005	0.014 ± 0.005	0.018 ± 0.005	<0.049	-
	SS	25,000	<1.2	<1.2	19	<2.9	-
MJD [32]	Cu	1,297	<0.0003	<0.0003	-	-	-
LUX [11]	Ti	230	<0.25	<0.2	-	<1.2	2.5
LZ (this work)	Ti	1,827	U_e <1.6 U_l <0.09	Th_e: 0.28 ± 0.03 Th_l: 0.23 ± 0.02	<0.02	<0.54	2.0 ± 0.1

tributes an additional ER background, due to the 'naked' beta emission from ^{214}Pb in the ^{222}Rn sub-chain. Background may also be generated from residual dust on the detector surfaces and plate-out of radon daughters, by emission of γ-rays from the radioactivity in the dust and neutrons from (α,n) reactions, as well as further radon emanation into the LXe from the dust, specifically from the inside of the inner vessel. Plate-out of radon progeny onto the surfaces of the cryostat following final cleaning post-manufacture must also be considered, especially the long-lived isotope ^{210}Pb. Daughters of ^{210}Pb, specifically ^{210}Po, can induce neutron emission through (α,n) reactions anywhere on the titanium surfaces, despite the relatively low α energy, generating additional nuclear recoil background. Furthermore, the presence of a reflective PTFE liner inside the inner vessel must also be considered; neutrons can also be induced here by α-particles from the cryostat, a process enhanced by the relatively high (α, n) cross section of the fluorine present in PTFE.

4.2. Background Modeling

Monte Carlo simulations have been performed to assess the contribution from all expected background sources, particularly those that generate single vertex interactions as expected from WIMP elastic scattering. These are conducted using LZSim, a simulation package constructed to model the experiment and inform the design, determine optimal performance parameters, and define tolerable rates from background sources. Developed using the GEANT4 toolkit [15], the framework inherits from the LUX model [33], and includes all parts of the experiment.

The LZ cryostat has been designed to stringent requirements that factor science goals, safety, containment, installation, and operation, and complies with ASME Boiler Pressure and Vessel Code (BPVC) VIII Div. 1 [34]. It will contain a total of 10 tonnes of LXe at a minimum temperature of −110°C and be placed inside a water tank for shielding purposes. There are three primary parts— the inner cryostat vessel (ICV), the outer cryostat vessel

(OCV) and the cryostat support (CS). Both the OCV and ICV contain a series of ports for cabling, liquid exchange and calibration sources. A CAD model of the cryostat is shown in Figure 1.

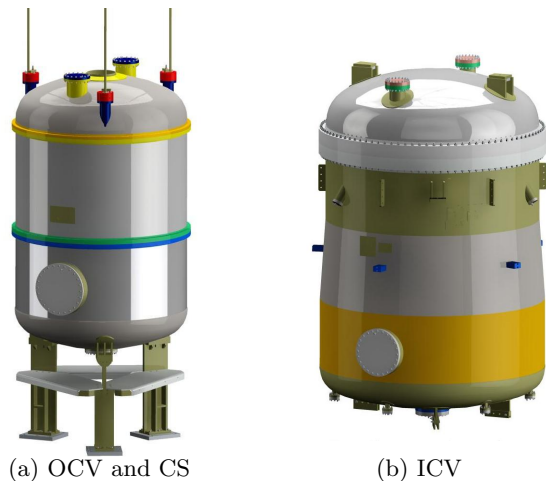(a) OCV and CS   (b) ICV

Figure 1: CAD models of the cryostat vessels and support. The OCV connects to three support legs mounted on baseplates and the ICV will be placed inside the OCV in vacuum. The full cryostat assembly stands 4.1 m tall.

4.3. Radioactivity Simulations

Simulations have been conducted by positioning radioactive nuclides in all the cryostat materials including the titanium, seals, liners, insulation, and bolts. For ER simulations, ^{60}Co, ^{40}K and the U and Th chain decays are simulated to produce γ-rays with the correct energies and branching ratios. For the U and Th early and late sub-chains, activities are assigned as determined by assays. Additionally, radon decays inside the LXe are simulated, under the assumption that all radon released from any material in contact with Xe mixes with the active mass.

For NR simulations, a neutron (α, n) energy spectrum for each material was obtained from SOURCES4A [35].

Single neutrons were emitted with energies sampled from the relevant spectrum, depending on their source material. The SOURCES4A code has been modified to extend the energies of α-particles up to 10 MeV from the original upper energy cut at 6.5 MeV [36], and to improve and extend the (α, n) cross-section library for a large number of materials [37–39], with newly added cross-sections calculated using the EMPIRE-2.19 code [40].

In principle, ^{238}U spontaneous fission can contribute to neutron yields significantly in materials where (α, n) rates are low. However, the near-simultaneous emission of up to 5 neutrons and up to 20 γ-rays results in highly efficient event rejection, reducing the contribution from spontaneous fission to negligible levels, and so these are removed from the background model [17].

The simulation output is analysed to examine events with energy depositions in the LXe active target. In particular, for an event to constitute a background count, the energy deposited in the active LXe must be within the WIMP search region of interest (6–30 keV recoil energy) and the particle must be observed to have scattered only once within the active LXe volume. Furthermore, LZ will have a veto detector external to the cryostat, and this may not register an energy deposition within an event time window.

Table VII summarises the materials used in the cryostat simulations, their masses, their measured activities, the neutron emission rate as determined with SOURCES4A for the given activities and mass, and the contribution to ER and NR background in LZ following the selection criteria. Figure 2 shows the spatial distribution of events generated by the cryostat radioactivity in the 7 tonne active volume and energy range of interest, showing the reduction as single scatter selection and vetoing is implemented.

4.4. Total Cryostat Background

The total expected background in LZ's 5.6 tonne fiducial mass in a 1,000-day exposure from the intrinsic radioactivity within the titanium of the cryostat is 0.0127 NR and 0.51 ER counts. Discrimination allows 99.5% rejection of ERs, reducing the cryostat contribution of WIMP-like events from ERs to 0.003 events. The NR background is also reduced to 0.006 counts under the standard NR acceptance of ~50% typically assumed in LXe TPC dark matter experiments. Figure 3 shows this background contribution together with that expected if a selection of alternative titanium samples were to be used based on our radioassay results. Also included is a hypothetical point based on radioactivity equal to the LUX cryostat material. The ER and NR background expected if any of the stainless steel samples were to be used for the LZ cryostat are also included. Contours on the figure indicate goals on background contribution from the cryostat material. The red contour represents 0.2 NR counts and an ER rate equivalent to 10% of the background expected from pp solar neutrino scattering in the active mass—one of the largest contributions to the ex-

periment. This marks the upper limit set on background from intrinsic radioactivity fixed in all materials in the LZ experiment. The yellow contour is 0.05 NR and 5% of the pp solar neutrino rate. Given the cryostat mass and proximity to the LXe, it is allocated up to a third of the maximum rate, 0.03 NR and 3.3% of the pp solar neutrino rate, denoted by the green contour. The TIMET samples produced with EBCH and 0% scrap and the LUX titanium each satisfy this goal. Although some of the stainless steel samples assayed would be acceptable, most either fail the requirement or are very close to failing, and all exceed rates from titanium. Furthermore, the large sample-to-sample variation indicates poorer reproducibility under standard manufacturing and processing. This presents increased risk of differences in radioactivities between assayed and procured material. The use of a stainless steel cryostat also reduces the efficiency of ER background vetoing, with γ-rays stopped in the vessels rather than penetrating to veto systems.

The ER and NR contributions from the intrinsic radioactivity fixed within all of the cryostat components is presented in Table VII. The combined contribution is 0.013 ± 0.001 NR and 0.63 ± 0.07 ER counts, reduced to 0.0032 ± 0.0004 WIMP like ER counts and 0.0065 ± 0.0005 NR counts after 50% NR acceptance and 99.5% ER discrimination.

Estimates of radon emanation from titanium have been made using emanation rates from steel in literature and conservative models of the reduction expected at cryogenic temperatures [41]. The total estimated activity from the titanium cryostat from ^{222}Rn is 0.15 mBq. This activity is combined with radon emanation from the dust on the inside of the ICV, assuming typical ^{238}U concentrations of $\approx$10 mBq/g and a surface density of 500 ng/cm^2, for a conservative total of 30 ER counts.

The contribution from intrinsic dust activity is insignificant, contributing only 1.5×10^{-4} NR counts and 7.6×10^{-3} ER counts. This was calculated assuming conservative exposure periods to air with no radon mitigation. Radon daughter plate-out, which leads to contamination of titanium surfaces with the long-lived isotope ^{210}Pb, can induce neutron emission through (α, n) reactions, but given the efficiency of neutron vetoing and the single scatter selection criteria in the fiducial volume, this process is expected to contribute only 2.8×10^{-3} NR counts.

The combined total activity from the cryostat including fixed radioactivity, radon emanation, plate-out and dust is 0.152 ER and 0.008 NR after discrimination and acceptances. Models of dust deposition are assumed to have a systematic uncertainty of 30%. These and the systematic uncertainty on radioassays of 10% are combined with statistical uncertainty from simulations to give a total of 0.160 ± 0.001(stat)± 0.030(sys) background counts to the WIMP search exposure of 5,600 tonne-days. The breakdown from the contributors to this total is presented in Table VIII.

Table VII: Table of expected backgrounds from all cryostat components, in an exposure of 5,600 tonne-days, before discrimination and NR acceptance is applied. The stainless steel is used for fasteners and calibration tubes, and the PEEK for seismic limiters. The totals show the mass weighed activities. ER and NR counts are rounded to two decimal places, and statistical uncertainties are given for the totals.

Name	Mass (kg)	^{238}U (mBq/kg) early	^{238}U (mBq/kg) late	^{232}Th (mBq/kg) early	^{232}Th (mBq/kg) late	^{60}Co (mBq/kg)	^{40}K (mBq/kg)	ER (cts)	NR (cts)
Titanium	2,292	1.59	0.11	0.29	0.25	0.00	0.54	0.51	1.27×10^{-2}
S. Steel	110.5	1.429	0.27	0.33	0.49	1.60	0.40	0.09	3.01×10^{-4}
PEEK	1.167	17.00	16.60	16.10	8.50	0.52	40.80	0.02	1.42×10^{-4}
Total	2,404	1.59	0.11	0.29	0.25	0.07	0.56	**0.63±0.06**	**0.013±0.001**

(a) Single scatter energy deposits.

(b) Single scatter energy deposits after vetoing.
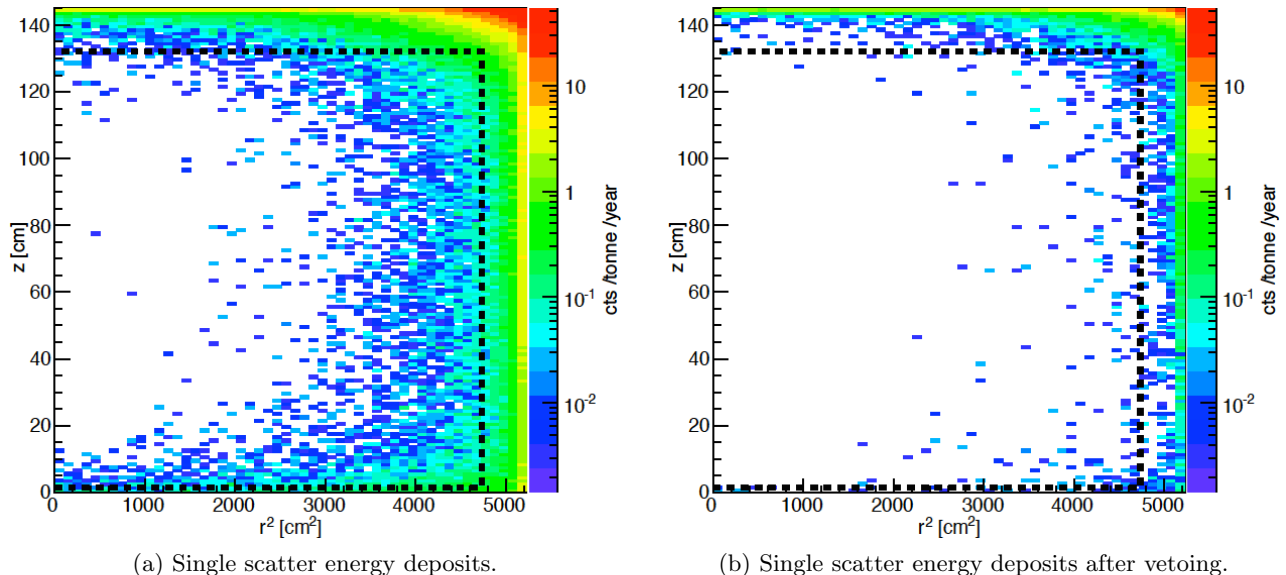
Figure 2: Expected background from the cryostat in LZ, showing the spatial distribution in r^2 and z within the active volume, and the fiducial volume (black dashed) that contains 5.6 tonnes of LXe. The colour scales are in counts/tonne/year. The effect of vetoing is highlighted through the reduction of events that satisfy single scatter selection in the energy range of interest for a WIMP search (left) by a factor ~ 10 when vetoes are implemented (right).

Table VIII: Breakdown of expected counts from the cryostat, in 5.6 tonnes of LXe and 1000 days; the total is shown before and after an ER discrimination of 99.5%, and an NR efficiency 50%.

	NR (cts)	ER (cts)
Titanium contamination	1.27×10^{-2}	0.51
Other contamination	4.43×10^{-4}	0.11
Rn emanation	0	29.7
Rn daughter plate-out	2.81×10^{-3}	0
Dust	1.51×10^{-4}	7.58×10^{-3}
Total (before dis./acc.)	0.016	30.31
Total (after dis./acc.)	**0.008**	**0.152**

5. Conclusion

The LZ collaboration has completed an R&D campaign to identify and procure radiopure titanium for construction of a double vessel cryostat. Material will also be used for construction of other internal detector components. We identified titanium made from EBCH melt with 0% scrap, produced by TIMET, as by far the best material. The measured activities for ^{238}U, ^{232}Th, and ^{60}Co from the sample are significantly lower than requirements and are, alongside the LUX titanium, the lowest reported in titanium to date.

Identification of low radioactivity titanium, together with associated manufacturing criteria required to reliably reproduce such activities, represents mitigation of a significant potential source of background for future dark matter experiments that will operate with metal cryostat vessels.

The total contribution to LZ backgrounds in the standard LZ exposure of 5.6 tons and 1000 days from the titanium vessels alone is 0.51 ER and 0.0107 NR, before any discrimination is applied. Accounting for all ancillary components and materials, and backgrounds that may be introduced during fabrication, assembly, and installation, the cryostat is expected to contribute a background of up to 0.152 ER and 0.008 NR WIMP-like background events to the LZ science run.
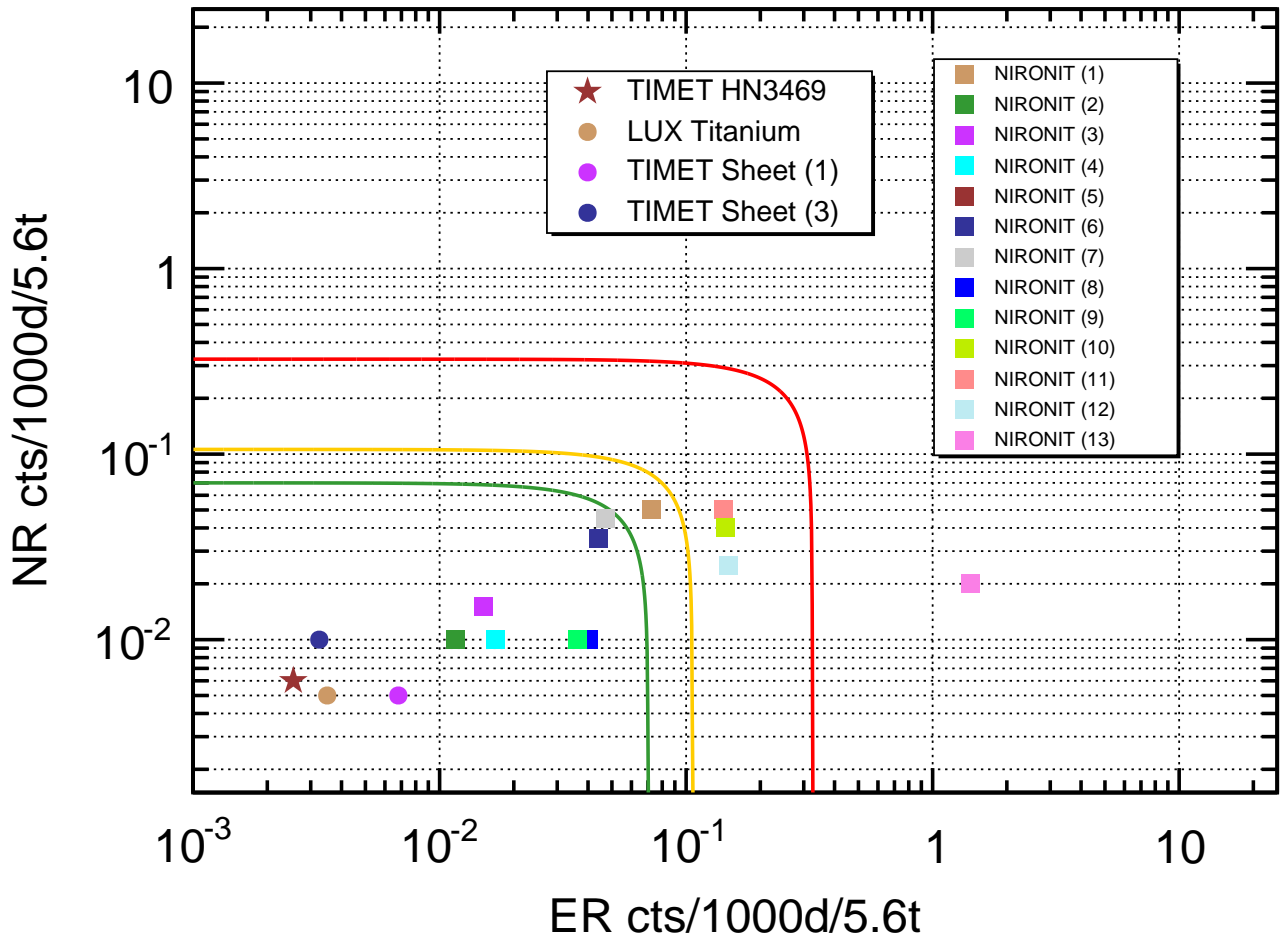
Figure 3: Expected background counts in ER and NR, within the fiducial volume after all vetoes are applied, showing the TIMET sample chosen for LZ, the screened stainless steel samples as well as the titanium used for the LUX cryostat. An NR acceptance of 50% and an ER discrimination factor of 99.5% are applied. The red curve corresponds to the sum of 10% of the pp solar neutrinos and 0.2 NR events, the yellow is the sum of 5% of the pp solar neutrino ER background and 0.05 NR events, and the green line is the sum of 3.3% of the pp solar neutrino ER background and 0.03 NR events. This green line was the requirement for the LZ cryostat, and the titanium chosen (indicated by the star) is well below this requirement.

conducted under the Ultra Sensitive Nuclear Measurements Initiative at Pacific Northwest National Laboratory, which is operated by Battelle for the U.S. Department of Energy under Contract No. DE-AC05-76RL01830.

[1] D. S. Akerib *et al.* (LZ), (2015), Conceptual Design Report; LBNL-190005, FERMILAB-TM-2621-AE-E-PPD, arXiv:1509.02910 [physics.ins-det].

[2] V. Chepel and H. Araújo, J. Instrum. **8**, R04001 (2013), arXiv:1207.2292 [physics.ins-det].

[3] V. N. Lebedenko *et al.* (ZEPLIN-III), Phys. Rev. Lett. **103**, 151302 (2009), arXiv:0901.4348 [hep-ex].

[4] D. Yu. Akimov *et al.* (ZEPLIN-III), Phys. Lett. **B709**, 14 (2012), arXiv:1110.4769 [astro-ph].

[5] W. Maneschg, M. Laubenstein, D. Budjas, W. Hampel, G. Heusser, K. T. Knopfle, B. Schwingenheuer, and H. Simgen (GERDA), Nucl. Instrum. Meth. **A593**, 448 (2008).

[6] C. Zhang, D. M. Mei, V. A. Kudryavtsev, and S. Fiorucci, Astropart. Phys. **84**, 62 (2016), arXiv:1603.00098 [physics.ins-det].

[7] D. S. Akerib *et al.* (LUX), Phys. Rev. Lett. **112**, 091303 (2014), arXiv:1310.8214 [astro-ph].

[8] D. S. Akerib *et al.* (LUX), Phys. Rev. Lett. **116**, 161301 (2016), arXiv:1512.03506 [astro-ph].

[9] D. S. Akerib *et al.* (LUX), Phys. Rev. Lett. **116**, 161302 (2016), arXiv:1602.03489 [hep-ex].

[10] D. S. Akerib *et al.* (LUX), Phys. Rev. Lett. **118**, 021303 (2017), arXiv:1608.07648 [astro-ph.CO].

[11] D. S. Akerib *et al.* (LUX), "Radio-assay of Titanium samples for the LUX Experiment," (2011), (unpublished), arXiv:1112.1376 [physics.ins-det].

[12] NSAC Subcommittee on Double Beta Decay, *Neutrinoless Double Beta Decay*, Tech. Rep. (Office of Science, U.S. Department of Energy, 1000 Independence Ave., SW, Washington, DC 20585, 2015).

[13] E. Mozhevitina, A. Chepurnov, A. Chub, I. Avetissov, V. Glebovsky, S. Nisi, M. L. d. Vacri, and Y. Suvorov, *Proceedings, 5th Topical Workshop on Low Radioactivity Techniques (LRT 2015): Seattle, WA, USA, March 18-20, 2015*, AIP Conf. Proc. **1672**, 050001 (2015).

[14] ASM International Handbook Committee, *ASM Handbook Volume 15: Casting* (ASM International, 9639 Kinsman Road, Materials Park, OH 44073-0002, 2008).

[15] S. Agostinelli *et al.* (GEANT4), Nucl. Instrum. Meth. **A506**, 250 (2003).

[16] D. C. Malling, S. Fiorucci, M. Pangilinan, J. J. Chapman, C. H. Faham, J. R. Verbus, and R. J. Gaitskell, "Dark Matter Search Backgrounds from Primordial Radionuclide Chain Disequilibrium," (2013), (unpublished), arXiv:1305.5183 [astro-ph].

[17] S. Shaw, *Dark Matter Searches with the LUX and LZ Dark Matter Experiments*, Ph.D. thesis, University College London (2016).

[18] VSMPO-AVISMA, (2015), Parkovaya St. 1, Verkhnaya Salda, Sverdlovsk Region, 624760, Russia.

[19] TIMET, (2015), 224 Valley Creek Blvd. Suite 200, Exton, PA 19341-2300.

[20] Supra Alloys, (2015), 351 Cortez Circle, Camarillo, CA 93012-8638, USA.

[21] "Honeywell Electronic Materials," (2015), 15128 E Euclid Ave, Spokane Valley, WA 99216-1801, USA.

[22] PTG - Performance Titanium Group, (2015), 8400 Miramar Rd Suite 200-248C San Diego, CA 92126-4387, USA.

[23] V. Álvarez *et al.* (NEXT), J. Instrum. **8**, T01002 (2013), arXiv:1211.3961 [physics.ins-det].

[24] NIRONIT Edelstahlhandel GmbH & Co. KG, (2015), Eckeler Strasse 10, D-21224 Rosengarten, Germany.

[25] E. Aprile *et al.* (XENON100), Phys. Rev. **D83**, 082001 (2011), [Erratum: Phys. Rev. **D85**, 029904 (2012)], arXiv:1101.3866 [astro-ph].

[26] TIMET, "HN3469-T Approved Certificate," (2016), Internal Report.

[27] C. E. Aalseth *et al.* (DarkSide), Adv. High Energy Phys. **2015**, 541362 (2015).

[28] E. Aprile *et al.* (XENON1T), JCAP **1604**, 027 (2016), arXiv:1512.07501 [physics.ins-det].

[29] H. M. Araújo *et al.* (ZEPLIN-III), Astropart. Phys. **35**, 495 (2012), arXiv:1104.3538 [physics.ins-det].

[30] M. Auger *et al.* (EXO-200), JINST. **7**, P05010 (2012).

[31] M. Agostini *et al.* (GERDA), Eur. Phys. J. **C74**, 2764 (2014), arXiv:1306.5084 [physics.ins-det].

[32] N. Abgrall *et al.* (Majorana), Nucl. Instrum. Meth. **A823**, 83 (2016), arXiv:1603.08483 [physics.ins-det].

[33] D. S. Akerib *et al.* (LUX), Nucl. Instrum. Meth. **A675**, 63 (2012), arXiv:1111.2074 [physics.data-an].

[34] Boiler and Pressure Vessel Committee, *ASME boiler and pressure vessel code, Section IX* (American Society of Mechanical Engineers, Two Park Avenue New York, NY 10016-59905, 2015).

[35] W. B. Wilson, R. T. Perry, W. S. Charlton, and T. A. Parish, Prog. Nucl. Energy **51**, 608 (2009), (SOURCES-4C).

[36] M. J. Carson *et al.*, Astropart. Phys. **21**, 667 (2004), arXiv:hep-ex/0404042 [hep-ex].

[37] R. Lemrani, M. Robinson, V. A. Kudryavtsev, M. De Jesus, G. Gerbier, and N. J. C. Spooner, Nucl. Instrum. Meth. **A560**, 454 (2006), arXiv:hep-ex/0601030 [hep-ex].

[38] V. Tomasello, V. A. Kudryavtsev, and M. Robinson, Nucl. Instrum. Meth. **A595**, 431 (2008), arXiv:0807.0851 [hep-ph].

[39] V. Tomasello, M. Robinson, and V. A. Kudryavtsev, Astropart. Phys. **34**, 70 (2010).

[40] M. Herman, R. Capote, B. Carlson, P. Oblozinsky, M. Sin, A. Trkov, H. Wienke, and V. Zerkin, Nucl. Data Sheets **108**, 2655 (2007).

[41] G. Zuzel, in *Topical Workshop on Low Radioactivity Techniques: LRT 2004.*, American Institute of Physics Conference Series, Vol. 785, edited by B. Cleveland, R. Ford, and M. Chen (2005) pp. 142–149, *Highly Sensitive Measurements of ^{222}Rn Diffusion and Emanation.*